Improved high-resolution EBSD analyses by correcting radial distortion of electron diffraction patterns

Qiwei Shi, Emeric Plancher, Dominique Loisnard, Phani Karamched, Liu Jun, Zhe Chen, Haowei Wang, Stéphane Roux

Improved high-resolution EBSD analyses by correcting radial distortion of electron diffraction patterns

Qiwei Shi[1,2], Emeric Plancher[3], Dominique Loisnard[4], Phani Karamched[5]
Jun Liu[2*], Zhe Chen[2*], Haowei Wang[2], Stéphane Roux[6]
1: SJTU-Paris Elite Institute of Technology,
Shanghai Jiao Tong University, Shanghai, 200240, China
2: School of Materials Science and Engineering,
Shanghai Jiao Tong University, Shanghai, 200240, China
3: Mines Saint-Étienne, Laboratoire Georges Friedel, UMR CNRS 5307,
158 cours Fauriel, 42100 Saint-Étienne, France
4: EdF R&D, Site des Renardières, avenue des Renardières,
Ecuelles, F-77818 Moret-sur-Loing, France
5: Department of Materials, University of Oxford, Parks Road, Oxford, United Kingdom
6: Université Paris-Saclay, CentraleSupélec, ENS Paris-Saclay, CNRS,
LMPS - Laboratoire de Mécanique Paris-Saclay, F-91190, Gif-sur-Yvette, France

Received: date / Accepted: date

Abstract

Registering experimental and simulated electron diffraction patterns is increasingly used for advanced electron backscatter diffraction indexation (EBSD) analysis, yet the accuracy of registration is limited by several effects not accounted for in pattern simulation, such as the Kikuchi band (K-band) asymmetry, gray level reversal and (mainly radial) optical distortion. Radial distortion parameters have previously been measured with chessboard-type standard samples. Simulated patterns have been adopted to demonstrate the necessity of optical distortion removal in EBSD analyses. However there still lacks an efficient and precise radial distortion assessment and correction method. Here a simple radial distortion model, including barrel and pincushion distortions, is proposed to rectify the diffraction patterns during EBSD analyses. The correlation between experimental pattern and the simulated master pattern permits to index the diffraction pattern and assess the radial distortion simultaneously. The method is applied to three high-definition experimental electron diffraction datasets acquired with different cameras. The radial distortion parameter is identified with a relative uncertainty below 4%. The consideration of radial distortion improves the correlation between experimental and simulated patterns. Gray level profiles of the K-bands are analyzed to verify the correctness of image registration. The current method provides a fast, economic yet precise correction of the radial distortion for advanced EBSD analyses.

Keyword: EBSD calibration, High-angular-resolution EBSD, Integrated digital image correlation, Optical distortion, Kikuchi band.

1 Introduction

Electron BackScatter Diffraction (EBSD) technique has evolved as a technique of choice to obtain crystallographic orientation fields in scanning electron microscopes. This technique aims principally at obtaining orientation maps from the analysis of the Kikuchi diffraction pattern (thereafter denoted as EBSP for Electron BackScatter Pattern) by Hough-transformation [1] or the newly emerged convolutional neural network [2] and dictionary approach [3]. Standard EBSD usually provides results with an angular resolution of about 0.5°. Such an uncertainty is sufficient to evaluate local orientation maps but cannot reveal elastic strains or small angle grain boundaries, which are associated with low deformations of diffraction images.

High-(angular) Resolution EBSD (HR-EBSD) — exploiting high-definition EBSPs registered onto a reference one through Digital Image Correlation (DIC) —has been proposed to obtain *relative* crystallographic orientations with a much higher accuracy [4, 5]. It has been shown that HR-EBSD enables the elastic strains to be measured with acceptable uncertainties and excellent spatial resolution [6]. Both *local* DIC algorithm based on cross-correlation [4] and *(integrated) global* DIC framework [7, 8, 9, 10] have been adopted in HR-EBSD. The latter method proves fast and precise for both simulated and experimental EBSPs. Global DIC can also measure grain-level absolute stress without simulated reference EBSP [11]. Yet, for both algorithms, the final results of HR-EBSD are limited by the accuracy of the projection parameters [12].

The calibration methods of EBSD projection parameters can be categorized as two groups: *hardware* and *software* based methods. The former relies on specific devices, such as a strain-free sample juxtaposed near the sample [13] and a movable detector [14, 15]. The basic idea of the increasingly popular software-based EBSD is to tune the projection parameters (and in particular the three coordinates of the PC) in order to maximize the similarity between experimental and *simulated* EBSPs, especially the *dynamically* simulated ones [16]. To match precisely the experimental and simulated patterns, many algorithms have been suggested, such as Nelder-Mead algorithm [17, 18, 19], cross-correlation with log-polar transform [20], evolution algorithm [21], SNOBFIT algorithm [19], global integrated-DIC (IDIC) algorithm [22] or non-disclosed ones used in commercial software [23]. The PC calibration uncertainty has been shown to reach values as low as 10^{-5} times the pattern width for simulated EBSPs. The reported Euler angles uncertainty is also very low: 0.03° for a 640×480 pixel EBSP used for the analysis of a tungsten carbide sample [24]. The same crystal orientation uncertainty level is obtained at grain boundaries for both grains [25].

However, different groups studying software EBSD calibration on polycrystal samples have recently reported grainwise discontinuity in PC fields [19, 22]. The shift of PC components across grain boundaries could reach 1-2 pixels, neither due to the sample topography nor due to the elastic strain. This intriguing phenomenon highlights the imperfection of registering experimental EBSP with a simple projection of simulated master pattern. Researchers have named several secondary effects in experimental EBSPs that need to be considered. If the secondary effects are not accounted for, *systematic* errors in PC and crystal orientation will be inevitable for software EBSD calibration

methods, regardless of the choice of optimisation algorithm. The brightness profile of Kikuchi bands is closely linked to the sample tilt angle [26]. The inhomogeneous distribution of diffracted electron energy influences the K-band width at different parts of the patterns [27], and IDIC has demonstrated its capability to identify the electron energies and thus provide better indexation results [28]. Kikuchi bands have brighter upper edges and darker lower ones, a phenomenon named excess-deficiency (abbreviated as ED hereinafter). This effect is due to the intuitively anisotropic diffracted electron distribution, a phenomenon well illustrated in Ref. [29] and partly solved recently [30]. The assessment and rectification of these secondary effects improves the EBSD indexation accuracy significantly.

Optical distortion also exists in EBSD detector, since, in conventional detectors, electron signals are transformed to optical ones. The imperfect optic lens result in numerous types of distortions, such as radial distortion, tangential distortion, misalignment between the optical axis and the phosphor screen, etc [31, 32]. Day [33] states that 8 independent parameters are needed to characterize the optical distortions, among which the radial distortion is the most significant and common one. Experimental EBSPs mostly suffer from barrel distortion, while pincushion distortion also exists. These two distortions correspond to cases where the magnification decreases or increases with the distance from the optical center, respectively. 'Barrel' and 'pincushion' are the figurative shapes of a square resulting from these distortions. Readers may refer to the slides in the supplementary document for illustrations of barrel distortion. Mingard *et al.* [32] measured systematically more than 10 detectors by chessboard-type standard samples, and found that most detectors of definition higher than 1 million pixels have a barrel distortion between 2×10^{-8} pix^{-2} and 4×10^{-8} pix^{-2}. Britton *et al.* [13] studied the effect of barrel distortion on elastic strain measurement, and demonstrates through a simulated dataset that the systematic error due to barrel distortion is above the noise floor of HR-EBSD. Tanaka *et al.* [21] studied the effect of radial distortion on PC calibration results on synthetic EBSD dataset, and found that PC_z is more disturbed than PC_x and PC_y. They also state that the radial distortion coefficient could be identified by the pattern matching between targeting EBSP and simulated ones, though without providing further details. Ernould *et al.* [34] proposed an algorithm to account for the optical distortion through a Gauss-Newton optimization method, and showed from simulated patterns that the optical distortion needs to be considered should elastic strain accuracy of order 10^{-4} be aimed at. However, a systematic assessment and correction of radial distortion for experimental EBSPs remain to be done, and a universal *software* correction strategy would be welcome. Direct EBSD detectors has the advantage of eliminating the electron/optic conversion, thus the optical distortion due to lens imperfection does not exist in theory. However, a previous study [35] showed that optical distortion could be significant due to the bad positioning of the tapered fibre bundle. This needs to be avoided for cameras using fiber-optic instead of lens, such as the 'Symmetry' detector of Oxford Instrument. As a result, correlating efficiently experimental EBSPs, with the presence of radial distortions, with simulated ones remain a challenge for the community.

The present work proposes to apply a radial distortion correction to the experimental EBSPs in order to minimize the difference between experimental and simulated EBSPs. Without using a specific sample for calibration, the proposed method simultaneously identifies the distortion parameter and calibrates the projection parameters via the IDIC framework. Section 2 details the proposed radial distortion assessment and correction. The effect of neglecting radial distortion on EBSD indexation is revealed by analysing simulated patterns. Sections 3-6 show

the algorithm performance on high-resolution backscatter and transmission electron diffraction patterns taken by 4 different cameras on 4 different samples. The improved HR-EBSD analysis results and K-band positioning prove the necessity of radial distortion correction. The results also demonstrate the algorithm's ability to identify and correct radial distortions.

2 Algorithm of IDIC-D to assess radial distortion

The projection geometry of EBSP is recalled in figure 1 together with the reference system used in the paper.

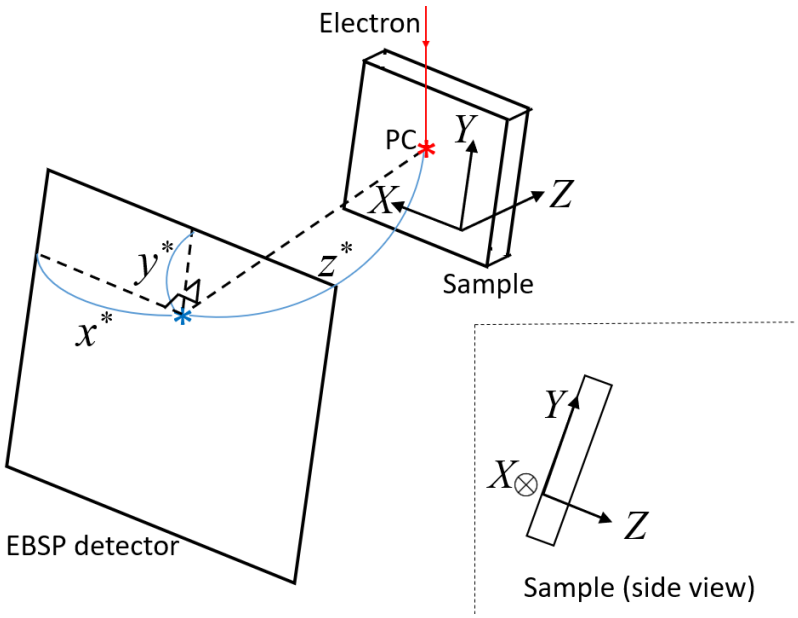

Figure 1: Coordinate systems (x, y, z) associated to EBSP detector and (X, Y, Z) associated to sample

Integrated Digital Image Correlation (IDIC) has been introduced to measure *directly* and *optimally* the geometric transformation of interest (or parameters quantifying it) from image registrations. The IDIC EBSD algorithm is primarily based on the assumption that only 6 projection parameters basically determine an EBSP for a given crystal, *i.e.,* the three coordinates of the projection center $\boldsymbol{x}^* = (x^*,\ y^*,\ z^*)$ and the three Euler angles $(\varphi_1, \phi, \varphi_2)$ of the crystal orientations. With the presence of radial distortion, the parameters characterizing it need to be incorporated into the IDIC framework. For perfectly centered lenses, the radial distortion is expressed as [36]

$$\delta_{\rho r} = \alpha\rho^3 + \beta\rho^5 + \gamma\rho^7 ... \tag{1}$$

Here ρ is the distance between the theoretical coordinate and the optic center of the lens, α, β, γ are the radial distortion parameters of different polynomial order, and $\delta_{\rho r}$ is the misplacement between the theoretical coordinate and the real coordinate of an experimental pattern. The radial distortion proportional to ρ^5 or higher order is generally negligible, thus we have explicitly in Cartesian coordinates the simplified radial distortion model:

$$(\boldsymbol{x} - \Delta\boldsymbol{x}_0) = (\hat{\boldsymbol{x}} - \Delta\boldsymbol{x}_0)(1 + \alpha\|\hat{\boldsymbol{x}} - \Delta\boldsymbol{x}_0\|^2) \tag{2}$$

where $\boldsymbol{x} = [x, y]$, with $z = 0$, is the pixel coordinates of the captured patterns, and $\hat{\boldsymbol{x}} = [\hat{x}, \hat{y}]$ are the distortion-free coordinates with the screen center as the origin, $\Delta\boldsymbol{x}_0 = [\Delta x_0, \Delta y_0]$ is the deviation of optical center from the pattern center. According to previous studies based on chessboard-type samples [15, 32], the center of radial distortion deviates from the center of diffraction pattern by at most a few dozen pixels. For the EBSP simulation with the presence of distortion, the coordinates x, y of each experimental pixel, instead of the distortion-free coordinates $\hat{x}, \hat{y}$, need to be mapped on the u, v directions of the master pattern.

The rest of the algorithm is similar to that for IDIC EBSD calibration, which is detailed in Ref. [22] and summarized here. Not to confuse it with the normal IDIC EBSD, the method described in the current paper is named as IDIC-D EBSD (Integrated Digital Image Correlation for Distorted EBSPs).

The EBSP screen is chosen as the reference defining the (x, y) plane, or $z = 0$. The unit vector $\boldsymbol{w}$ linking the pattern center to each pixel $\boldsymbol{x}$ of the screen can be expressed as

$$\boldsymbol{w} = \frac{(\boldsymbol{x} - \boldsymbol{x}^*)}{|\boldsymbol{x} - \boldsymbol{x}^*|} \tag{3}$$

In order to rotate this vector from the screen frame of reference $\boldsymbol{w}$ to that of the spherical master pattern, $\boldsymbol{v}$, one should multiply it by a rotation operator $\boldsymbol{Q}$

$$\boldsymbol{v} = \boldsymbol{Q}\boldsymbol{w} \tag{4}$$

whose expression, using the Euler angles, reads in Bunge notations:

$$\boldsymbol{Q} = \begin{bmatrix} \cos\varphi_1 \cos\varphi_2 - \sin\varphi_1 \sin\varphi_2 \cos\phi & \sin\varphi_1 \cos\varphi_2 + \cos\varphi_1 \sin\varphi_2 \cos\phi & \sin\varphi_2 \sin\phi \\ -\cos\varphi_1 \sin\varphi_2 - \sin\varphi_1 \cos\varphi_2 \cos\phi & -\sin\varphi_1 \sin\varphi_2 + \cos\varphi_1 \cos\varphi_2 \cos\phi & \cos\varphi_2 \sin\phi \\ \sin\varphi_1 \sin\phi & -\cos\varphi_1 \sin\phi & \cos\phi \end{bmatrix} \tag{5}$$

The stereographic projection of $\boldsymbol{v}$ onto the master pattern plane, $\boldsymbol{u}$, is written

$$\boldsymbol{u} = \frac{\boldsymbol{v} - \boldsymbol{n}}{(1 - \boldsymbol{v}.\boldsymbol{n})} + \boldsymbol{n} \tag{6}$$

where $\boldsymbol{n} = (0, 0, 1)^\top$ denotes the unit vector pointing at the north pole. An illustration of the stereographic projection and the geometric relations between vectors $\boldsymbol{u}, \boldsymbol{v}, \boldsymbol{w}$ are provided in Ref. [22]. Thus the projected position, $\boldsymbol{u}(\boldsymbol{x})$, on the master pattern can be expressed explicitly as a function of $\boldsymbol{x}$ and of the projection parameters $(\varphi_1, \phi, \varphi_2, x^*, y^*, z^*, \alpha, \Delta x_0, \Delta y_0)$ collectively noted as $\boldsymbol{P}$, a total of 9 parameters.

In IDIC-D EBSD algorithm, experimental EBSP is taken as $f(\boldsymbol{x})$ and the dynamically simulated EBSP master pattern is $g(\boldsymbol{u})$. Therefore the corrected simulated pattern corresponds to $g_{\boldsymbol{u}}(\boldsymbol{x}) = g(\boldsymbol{u}(\boldsymbol{x}, \boldsymbol{P}))$. The IDIC-D algorithm involves matching at best $f(\boldsymbol{x})$ and $g_{\boldsymbol{u}}(\boldsymbol{x})$, through the minimization of a quadratic norm of the residual r summed over the entire ROI. The cost function to minimize is written

$$\Theta = \sum_{ROI} \omega(\boldsymbol{x})^2 r^2(\boldsymbol{x}) = \sum_{ROI} \omega(\boldsymbol{x})^2 \left[f(\boldsymbol{x}) - g_u(\boldsymbol{x})\right]^2 \tag{7}$$

where $\omega(\boldsymbol{x})$ is the weight associated to each pixel $\boldsymbol{x}$, $g_u(\boldsymbol{x})$ is the current estimate of simulated EBSP during iterative algorithms. The weights ω are introduced here as they may be used to make this functional *optimal* with respect to the handling of noise [22]. For high quality EBSPs where the noise is low for the entire pattern, ω could be set uniformly 1, as done in the present work if not stated otherwise explicitly. The minimization of the cost function

leads to successive corrections of the transformation $\boldsymbol{u}(\boldsymbol{x})$ estimation until convergence [37]. The cost function (7) is iteratively minimized with a Gauss-Newton algorithm. The initial parameters could be the Euler angle triplet and PC coordinates provided by commercial Hough indexation, or the calibration results by IDIC6-EBSD. The initial parameter α could be set to 0. Starting from this approximate solution, the transformation $\boldsymbol{u}(\boldsymbol{x})$ is progressively corrected with linear combinations of sensitivity fields constituting the kinematic basis.

A slight modification of any parameter δP_i, induces a modification of the simulated image as

$$\delta g_u(\boldsymbol{x}) = \nabla g(\boldsymbol{u}) \cdot \frac{\partial \boldsymbol{u}(\boldsymbol{x}, \boldsymbol{P})}{\partial P_i} \delta P_i \tag{8}$$

The parameters $\varphi_1, \phi, \varphi_2, x^*, y^*, z^*$ are of order 1, while α is normally of order 10^{-8} pix^{-2}. α is normalized to the order of 1 in the code for numerical stability reasons, especially for the calculation of the sensitivity field with respect to α.

The column vector $\{\boldsymbol{\delta P}\}$ gathering all corrections to $\boldsymbol{P}$ is obtained from the solution of the linear system

$$[\boldsymbol{M}]\{\boldsymbol{\delta P}\} = \{\boldsymbol{\gamma}\} \tag{9}$$

where $[\boldsymbol{M}]$ is the approximated Hessian matrix for Gauss-Newton optimization at iteration $n-1$

$$M_{ij}^{(n-1)} \equiv \frac{\partial \sum_{ROI} \omega(\boldsymbol{x}) \left[f(\boldsymbol{x}) - g_u(\boldsymbol{x}) \right]}{\partial P_i} \frac{\partial \sum_{ROI} \omega(\boldsymbol{x}) \left[f(\boldsymbol{x}) - g_u(\boldsymbol{x}) \right]}{\partial P_j} \tag{10}$$

or more explicitly

$$M_{ij}^{(n-1)} = \sum_{ROI} \omega(\boldsymbol{x}) \left[\nabla_{u_1} g(\boldsymbol{u}) \frac{\partial u_1(\boldsymbol{x}, \boldsymbol{P})}{\partial P_i} + \nabla_{u_2} g(\boldsymbol{u}) \frac{\partial u_2(\boldsymbol{x}, \boldsymbol{P})}{\partial P_i} \right] \sum_{ROI} \omega(\boldsymbol{x}) \left[\nabla_{u_1} g(\boldsymbol{u}) \frac{\partial u_1(\boldsymbol{x}, \boldsymbol{P})}{\partial P_j} + \nabla_{u_2} g(\boldsymbol{u}) \frac{\partial u_2(\boldsymbol{x}, \boldsymbol{P})}{\partial P_j} \right] \tag{11}$$

Here $[\boldsymbol{M}]$ is a symmetrical matrix, whose dimension is the number of parameters to be calibrated. The second member $\{\boldsymbol{\gamma}_i\}$ includes the residual field

$$\gamma_i^{(n)} \equiv \frac{\partial \Theta}{\partial P_i} \tag{12}$$

The explicit expressions of $[\boldsymbol{M}]$ and $\{\boldsymbol{\gamma}_i\}$ can be derived by the chain rule without special difficulties (thus not fully detailed here).

When $\|\{\boldsymbol{\delta P}\}\| < \epsilon$, ϵ being chosen equal to 10^{-6} for all the calculations of this paper, the minimization stops and $\boldsymbol{P}$ is stored. Otherwise, $\boldsymbol{P}$ is updated

$$\boldsymbol{P}^{(n)} = \boldsymbol{P}^{(n-1)} + \boldsymbol{\delta P}^{(n)} \tag{13}$$

Once $\boldsymbol{P}$ is obtained, the simulated EBSP resembles the reference experimental EBSP at best. The radial distortion is assessed at the same time of EBSP indexation.

Table 1 lists the targeting parameters of several versions of IDIC and IDIC-D. The number in the version name indicates the degrees of freedom of the indexation. For the EBSPs of an EBSD scan, the projection center coordinates x^*, y^*, z^* are regularly positioned, and the values of radial distortion parameter α should be identical. This feature allows the regularization of these parameters [22]. For example, α can be calibrated for each camera, and then be fixed for all the diffraction patterns recorded by it. Note that although IDIC3 and IDIC-D3 only identify the Euler angle triplet, the parameter α still intervenes in IDIC-D3 calculation. Besides, IDIC is the special

case of IDIC-D when α equals 0. The iteration numbers at convergence and the execution time on a Dell laptop with Intel i7-10750H CPU for each IDIC version are also listed in Table 1. To give a fair evaluation of the calculation speed, the Euler angle triplet in the initialization is deliberately set to be 0.05° away from the value at convergence, and the full definition 2048×2048 EBSP is used in the evaluation. A comparison of the indexation precision of each version of IDIC and IDIC-D will be provided in Section 4.

Table 1: List of calibrated parameters for different versions of IDIC methods.

Indexation algorithm	List of calibrated parameters	Iterations at convergence	Execution time (s)
IDIC6	$(\varphi_1, \phi, \varphi_2, x^*, y^*, z^*)$	14	32
IDIC3	$(\varphi_1, \phi, \varphi_2)$	10	16
IDIC-D9	$(\varphi_1, \phi, \varphi_2, x^*, y^*, z^*, \alpha, \Delta x_0, \Delta y_0)$	62	208
IDIC-D7	$(\varphi_1, \phi, \varphi_2, x^*, y^*, z^*, \alpha)$	48	135
IDIC-D6	$(\varphi_1, \phi, \varphi_2, x^*, y^*, z^*)$	26	76
IDIC-D4	$(\varphi_1, \phi, \varphi_2, \alpha)$	24	51
IDIC-D3	$(\varphi_1, \phi, \varphi_2)$	14	23

2.1 IDIC-D example on simulated patterns

Figure 2 displays 3 simulated EBSPs, corresponding to distortion parameters $-1 \times 10^{-7}, 0, 1 \times 10^{-7}$ pix^{-2} respectively. Note that $\pm 1 \times 10^{-7}$ pix^{-2} is a radial distortion level higher than that of most commercial cameras, and it is chosen to make the distortion effect more visible. The central line of the Kikuchi bands are drawn on top of EBSPs in order to highlight the optical distortions. The dashed lines correspond to the diffracting plane on EBSPs neglecting radial distortion, and the solid lines indicate the diffracting plane when the radial distortion is incorporated. The dashed lines are straight, while the solid lines have 'barrel' or 'pincushion' shapes depending on the α values. For these simulated EBSPs, the calculated diffracting plane traces with radial distortion lie in the center of K-bands. Whether the diffracting plane traces coincide with the K-band central line constitutes a direct and visual criteria for the quality of EBSP indexation. This criterion will be used on experimental patterns in the current paper.

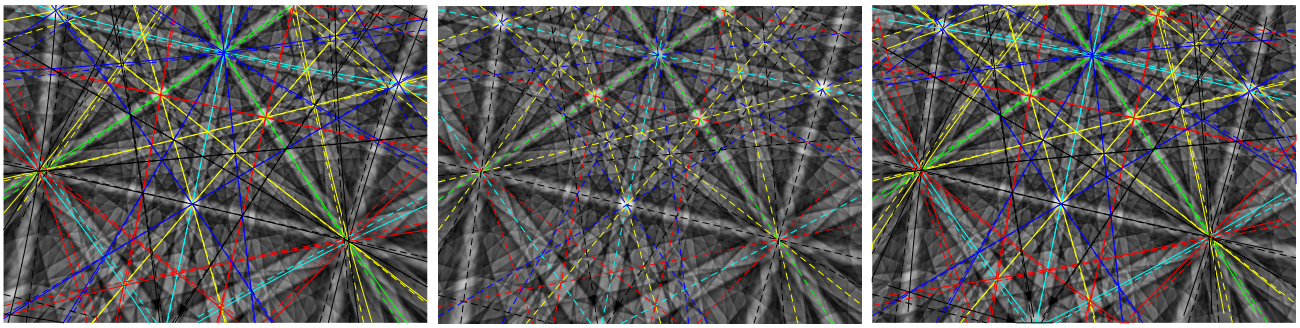

(a) (b) (c)

Figure 2: Illustration of the effect of radial distortion on EBSPs with different values of the distortion parameter α. (a) $\alpha = -1 \times 10^{-7}$ pix^{-2}; (b) $\alpha = 0$ pix^{-2}, (c) $\alpha = 1 \times 10^{-7}$ pix^{-2}. The dashed lines correspond to diffracting planes without radial distortion, and the solid lines with radial distortion incorporated.

In most cases, the radial distortion is not considered in EBSD indexation and calibration. Let us first study the effect of induced consequences on EBSD calibration results. Simulated diffraction patterns of different α values are generated for calibration. Two crystal orientations, corresponding to the two top grains shown in Figure 10a, are used to generate the patterns, and the IDIC EBSD algorithm without radial distortion correction is used to index them. The deviation from the true values of the 6 parameters $\boldsymbol{P}$ are shown in Figure 3, with each sub-figure plots the result of simulated patterns of one crystal orientation. The misorientation due to neglect of radial distortion is expressed in Rodrigues' vector $(\omega_X, \omega_Y, \omega_Z)$, whose components describe the rotation along the X, Y, Z directions of the sample respectively. α affects the EBSD calibration results in a different manner: z^* has a clear trend with α, but the other 5 parameters do not deviate from the true value in the same direction. Positive α values of barrel distortion shrink the EBSP [21], especially near the corners. As a result, EBSD calibration without correcting α will underestimate the z^* parameter. For full resolution (1600×1200) EBSPs with common barrel distortions ($\alpha = 2 \times 10^{-8}$ pix^{-2}), EBSD calibration without correcting the radial distortion underestimate the sample-detector distance by 6-10 pixels (or 120-200 microns). Neglecting radial distortion influences the other 5 parameters to a lesser degree in different ways, depending on the crystal orientations, and cannot be categorized simply.

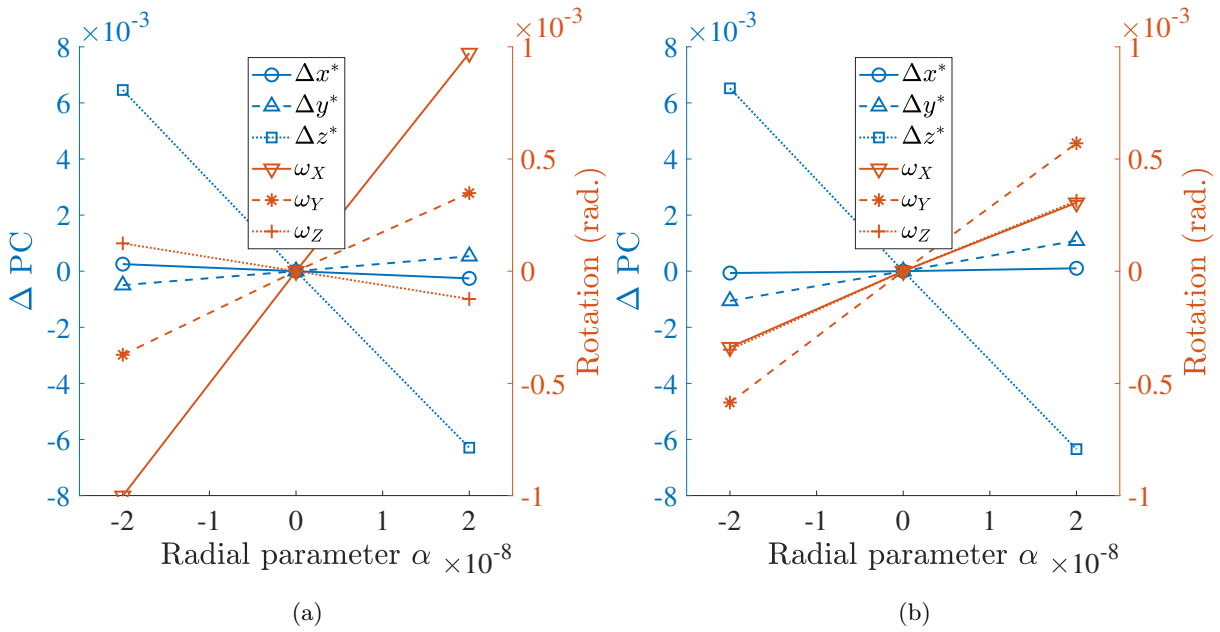

Figure 3: Effect of barrel distortion on EBSPs to EBSD calibration on Euler angles and projection center coordinates when the pattern distortion is not corrected. Sub-figures (a) and (b) correspond to the results using the crystal orientations of two grains of an Al-Mg alloy.

The method IDIC-D once again demonstrates the high extendibility of integrated digital image correlation in EBSD analyses. The radial distortion parameter adds to the growing list of accessible physical quantities by IDIC-EBSD: displacement gradient tensor [7, 8, 9], Euler angle triplet and projection center coordinates [22], overlapping Kikuchi bands at grain boundaries [25], distribution of heterogeneous electron energies of EBSPs [28]. Whenever a physical quantity can be incorporated in the (efficient) generation of a simulated EBSP from pre-calculated master patterns, it can be identified via the correlation with the experimental patterns.

This numerical study on synthetic data shows the importance of radial distortion correction in HR-EBSD analyses. The method IDIC-D is then tested on experimental diffraction patterns taken by 4 different cameras at different laboratories. The full details and discussions are provided in the following three sections respectively.

3 Test on EBSPs by a camera HR4M

The high-definition EBSPs around a triple joint, taken by a camera HR4M with 2048×2048 pixels and reported in Ref. [9], are analyzed by the current method. The sample is an A316 stainless steel after 0.3% tensile deformation.

Figure 4 shows the radial distortion center deviation $(\Delta x_0, \Delta y_0)$ calibrated by IDIC-D9. More than 100 EBSPs are calibrated for each grain. Both Δx_0 and Δy_0 are centered around 0, which is consistent with the reported characterization of radial distortions [32]. The uncertainty level of $(\Delta x_0, \Delta y_0)$ is large, around 35 pixels, which is not precise enough to measure the $\Delta \boldsymbol{x}_0$ of order 5-50 pixels according to [32]. Besides, their distribution is correlated with the crystal orientation as shown in Figure 4, which was unexpected. The high uncertainty level of $(\Delta x_0, \Delta y_0)$ and the large time cost of IDIC-D9 show that 9 degrees of freedom is beyond the limit of IDIC EBSD

calibration with reasonable precision. As shown in Equation 2, the distortion displacement $(x - \hat{x}, y - \hat{y})$ with $(\Delta x_0, \Delta y_0)$ of the order 10^{-2} of pattern width does not differ much from the case of $\Delta x_0 = \Delta y_0 = 0$. For example, the $\alpha \approx 7 \times 10^{-9}$ pix^{-2} measured for this HR4M camera leads to 21.3 pixels displacement at the EBSP corner assuming $\Delta x_0 = \Delta y_0 = 0$. The displacement value increases to 23.5 pixels if $\Delta x_0 = \Delta y_0 = 35$ pix. Their difference is about 10% for the corner, where the radial distortion effect is the most eminent. Moreover this difference averages out to 0 when integrated along the polar angle. As a result, for all the following calculations, both Δx_0 and Δy_0 are set as 0, to enhance the result uncertainty of the more important parameters $(\varphi_1, \phi, \varphi_2, x^*, y^*, z^*, \alpha)$.

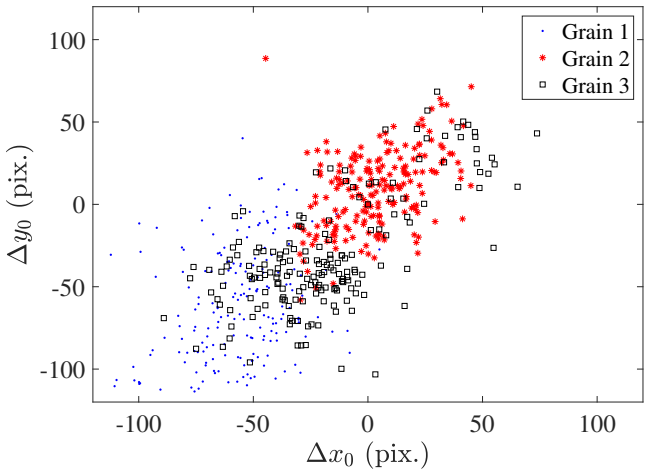

Figure 4: The calibrated radial distortion center deviation $(\Delta x_0, \Delta y_0)$ by IDIC-D9.

Figure 5 shows the calibration results. Figures 5a-5c are the PC components calibrated by IDIC6. The discontinuities of x^* at the grain 1&3 and 2&3 boundaries, and the y^* jump at the grain 1&2 border are clearly visible. Figure 5d plots the calibrated radial distortion parameter α by IDIC-D7. α oscillates around 7.28×10^{-9} pix^{-2} with a standard deviation of 0.42×10^{-9} pix^{-2}. The variation of α exists both inside the same grain, and across different grains. By fixing α to 7.28×10^{-9} pix^{-2}, the calibration algorithm of version IDIC-D6 is rerun on the dataset, and Figures 5f-5h show its calibrated PC fields. By considering the barrel distortion, the continuity of both x^* and y^* fields improves significantly, which demonstrates the benefits of correcting the radial distortion. Besides, the z^* field increases by about 6 pixels uniformly, similar to the virtual test shown in Figure 3.

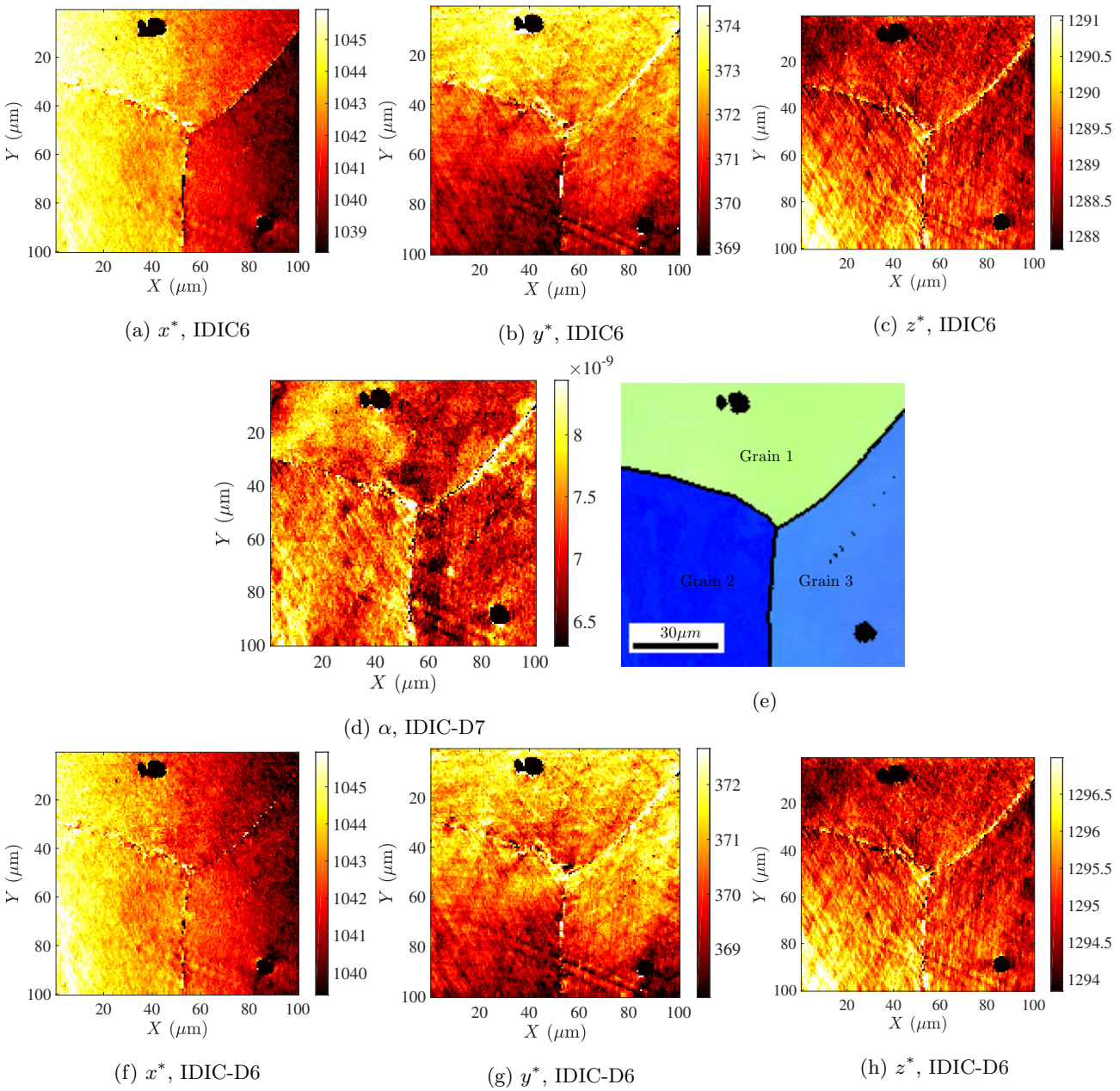

(a) x^*, IDIC6 (b) y^*, IDIC6 (c) z^*, IDIC6

(d) α, IDIC-D7 (e)

(f) x^*, IDIC-D6 (g) y^*, IDIC-D6 (h) z^*, IDIC-D6

Figure 5: Projection parameters calibration results for the triple-joint dataset. (a-c) The projection center coordinate components calibrated by IDIC6. (d) The radial parameter α calibrated by IDIC-D7. (e) The inverse pole figure of the dataset, with the numeration of 3 grains. (f-h) The PC fields by IDIC-D6, while α is set as 7.28×10^{-9} pix^{-2}.

4 Test on EBSPs taken by a Nordlys II camera

The bending test reported in Refs. [38, 39, 9] is analysed in the current work. The details of the experiment are listed in the Appendix. 5000 full resolution EBSPs are recorded by an Oxford NordlysII camera.

Figure 6 shows an example of IDIC-D EBSD calibration on experimental EBSP. Figure 6a shows the EBSP

indexed by IDIC-D7. The straight dashed lines and curvy solid lines indicate the diffracting planes calculated without and with radial distortions respectively. A close look reveals that the curvy solid lines stitch to the Kikuchi band center better than the dashed lines, especially for the horizontal band near the top. Figure 6b plots the master pattern simulated by EMsoft [40], with blue lines marking the projection area used for generating the simulated EBSP without considering radial distortion. Let us underline that the bulging shape of the blue lines has nothing to do with barrel distortion, but due to the stereographic projection from a sphere to a 2D plane. The black lines mark the projection area using the parameters given by IDIC-D7 method. Note that the radial distortion parameter is amplified by 10 to highlight the difference between the two projection regions. The radial distortion has a bigger impact on corner regions. Figuratively, the barrel distortion compacts some information outside the normal visual field into the detector, especially for the peripheral areas. To mimic this effect, IDIC-D enlarges the projection area according to the barrel distortion model, as shown in Figure 6b. The residual map between the experimental pattern and the projected pattern with IDIC-D parameters is shown in Figure 6c. The residual is far from pure noise, as can be seen from the clear presence of several bands. The excess-deficit effect is also visible in the residual map. The high residual level shows that the EBSP simulation does not account for all the effects in experimental EBSP formation, yet the good positioning of Kikuchi bands indicates a correct indexation. Besides, the continual improvement of the residual (*i.e.,* the drop of residual norm) guides the way to better HR-EBSD analyses.

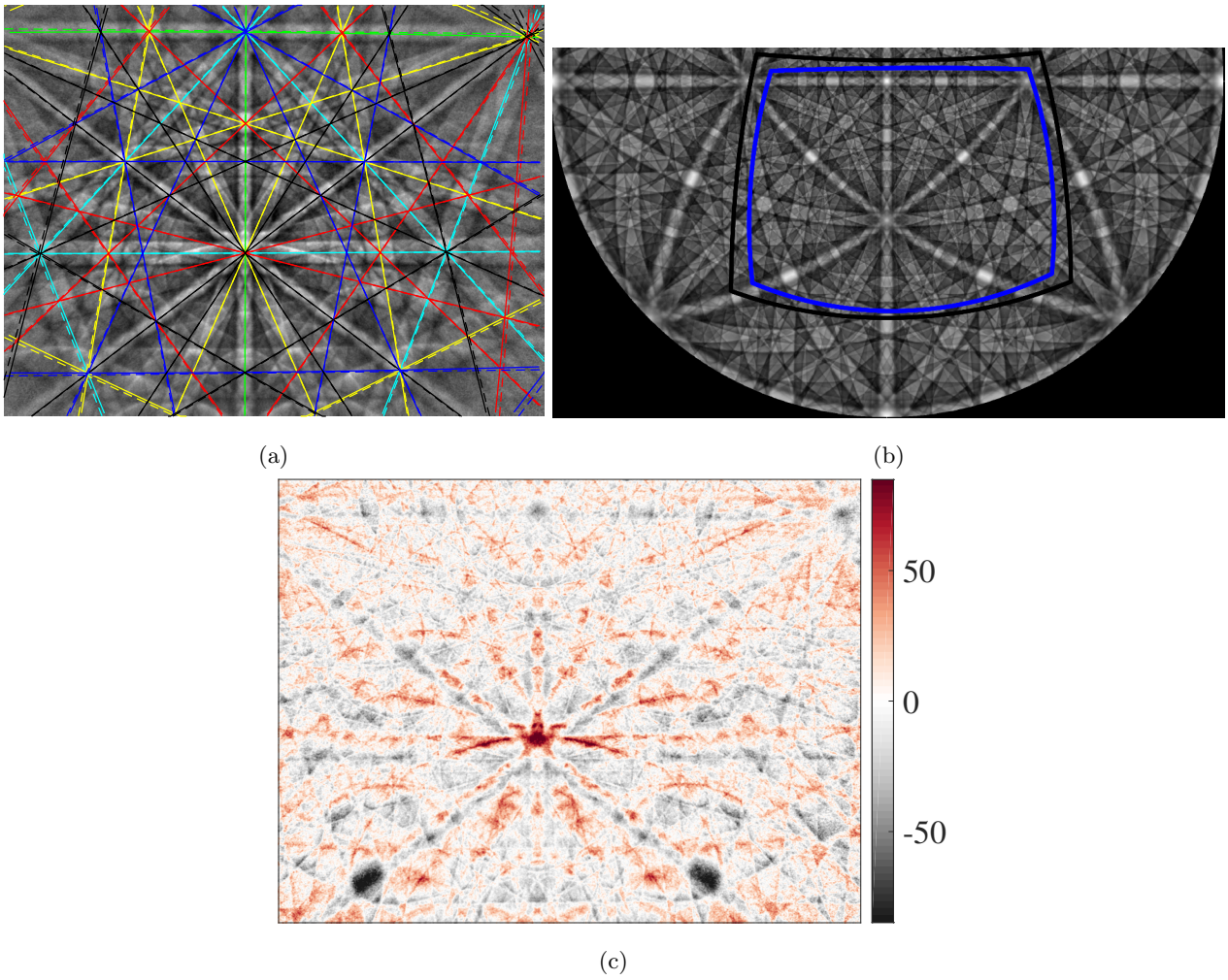

Figure 6: An example of IDIC-D EBSD calibration on experimental image. (a) Experimental EBSP of size 1024×1344; (b) The stereographically projected region of master pattern to generate the simulated EBSP. The blue line marks the region predicted by IDIC calibration method, and the black region by IDIC-D7 method with radial distortion magnified by 10 to highlight the differences. (c) Residual map $r(\boldsymbol{x})$ between the experimental pattern and the simulated one with IDIC-D parameters.

Figure 7 shows the calibration results for the entire line scan. The radial parameter α is consistently around 3.08×10^{-8} pix^{-2} for this dataset. This distortion level is consistent with the evaluations reported by Mingard *et al.* [32]. In fact, α was evaluated as 3.2×10^{-8} pix^{-2} for this camera thanks to a chessboard-type sample [15, 32]. This mere 4% contrast cross-validates the accuracy of the IDIC-D method. Figure 7b compares the image correlation residuals of the IDIC3 and IDIC-D3 methods. The average residual of IDIC-D3 is 3.5% lower than IDIC3. This seemingly small amount is actually very significant, given the high gray level contrast between experimental and simulated EBSPs shown in Figure 6c. This demonstrates both the precision and necessity of the proposed IDIC-D distortion correction framework. Figures 7c-7e show the contrast of projection center calibration results when distortion is included or not in the IDIC framework. z^* is consistently 0.005 (or 6 pixels) larger when distortion is considered, meaning that the underestimation of z^* is corrected. Figure 7c shows a linear trend due to the beam

shift. The uncertainty level is roughly the same for IDIC and IDIC-D7, showing that the IDIC framework handles well one additional degree of freedom. The fluctuations of y^*, z^* show that the projection center calibration is slightly impacted by the strain state of the sample, which is confirmed by previous studies [41, 22].

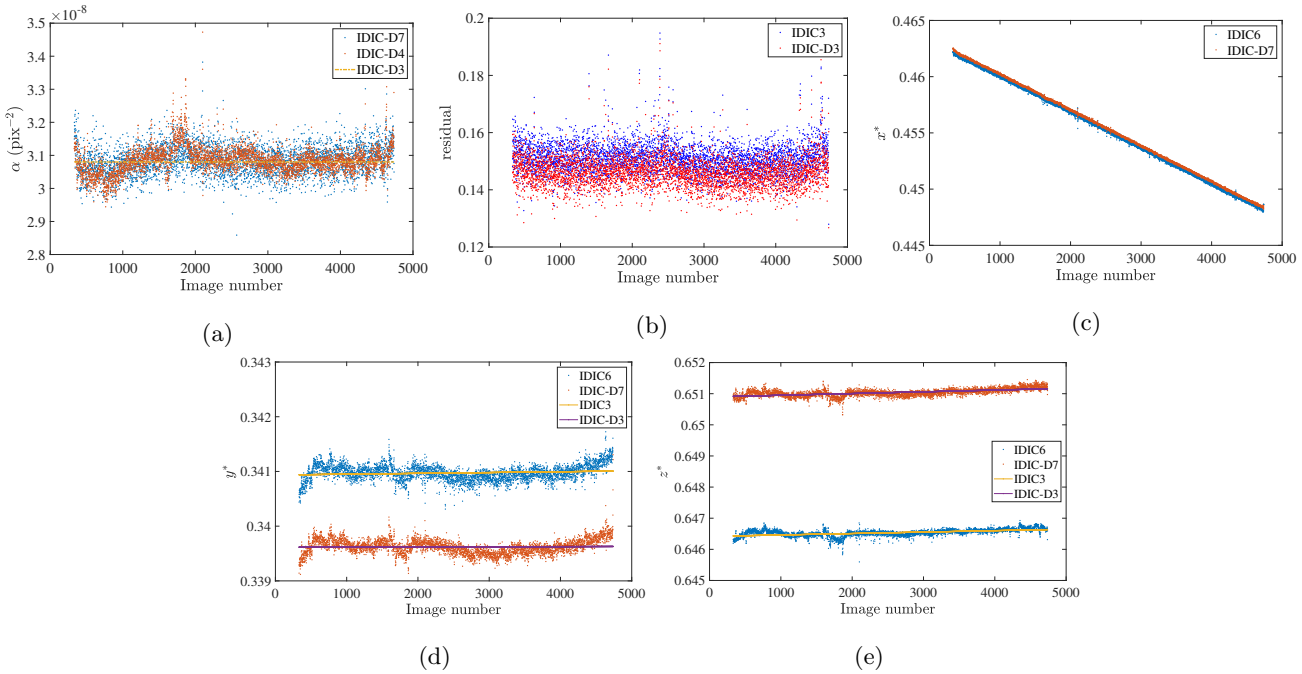

Figure 7: Calibration result profiles of IDIC and IDIC-D on the same EBSD line scan data. (a) Calibrated barrel parameter α; (b) Residuals of image correlations; Projection center coordinates x^* (c), y^* (d), z^* (e).

Let us now compare indexed orientation by different methods. As the sample is single crystal and slightly strained, and the step size 100 nm is small, the true misorientation between neighboring acquisition points is assumed to be 0. As a result, the indexed misorientation of neighboring points is a metric of indexation uncertainty. The distributions of misorientation of neighboring pixels, indexed by 5 different versions of IDIC and IDIC-D algorithms, are plotted in Figure 8a. Though IDIC-D7 calibrates 7 parameters simultaneously, it results in better crystal orientation precision than the IDIC6 algorithm with 6 degrees of freedom. This highlights the benefits of radial distortion correction on crystal orientation indexation. Besides, IDIC-D3 results in the same precision as IDIC-D4, and they perform slightly better than IDIC3 in terms of indexation precision, as the median misorientation angles are 0.00283° and 0.00309°, respectively.

Figure 8b plots the misorientation of the crystal orientations indexed by IDIC3 and IDIC-D3. The misorientation level around 0.05° is negligible for conventional EBSD analyses, but needs to be treated properly in HR-EBSD characterizations.

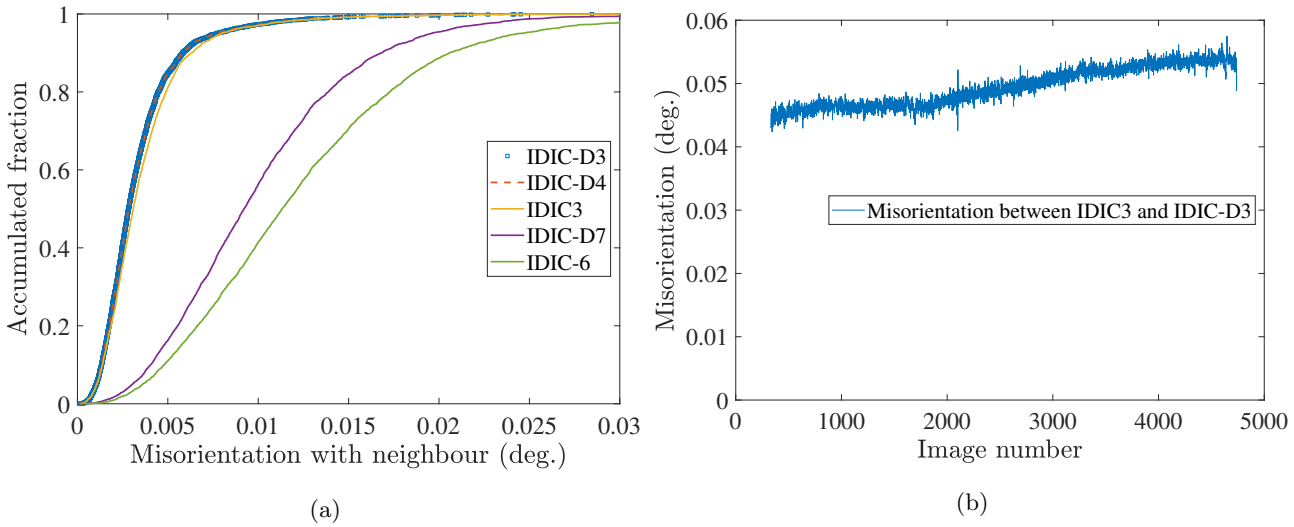

(a) (b)

Figure 8: (a) The distribution of misorientation with neighboring pixels, calculated with indexation results of IDIC and IDIC-D with different degrees of freedom. (b) The misorientation of the crystal orientation indexed by IDIC3 and IDIC-D3 methods.

A persistent problem of the technique HR-EBSD is the existence of strain-free reference pattern. Numerous studies have been devoted to the search of best reference experimental EBSP [42], or to the practice of HR-EBSD with simulated reference patterns [43, 44, 21]. The correction of possible barrel distortion would be an absolute necessity in the latter case.

Figure 9 compares the estimated elastic strain components for the 5000 EBSPs with simulated reference pattern when the barrel distortion is corrected or not. The out of plane stress component σ_{zz} is adjusted to 0 to fix the isotropic dilatation. For these slightly and differently deformed patterns (strain of order 10^{-4} according to [38]), the correction of radial distortion reduces the estimated elastic strain by 20-30%. Besides, the uncertainty of the strain components is lower when using the reference pattern given by IDIC-D3. This result proves the necessity of barrel distortion correction. The remaining error is due to other imperfections not modelled here, such as the excess-deficiency effect of horizontal Kikuchi bands, the inability to simulate all the minute details of experimental EBSP, the inaccuracy of projection parameters, and the oversimplification of the well-centered pure-3rd-order radial distortion model adopted here.

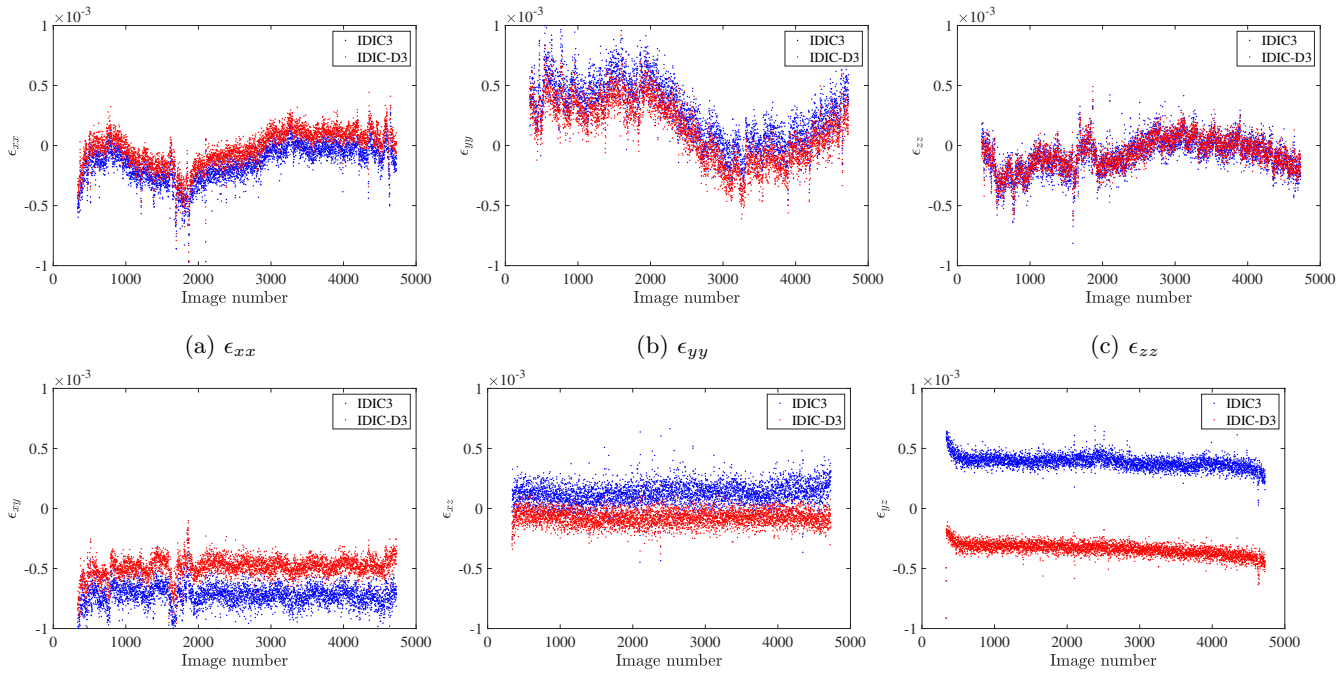

(a) ϵ_{xx} (b) ϵ_{yy} (c) ϵ_{zz}

(d) ϵ_{xy} (e) ϵ_{xz} (f) ϵ_{yz}

Figure 9: The estimated strain components for the 5000 EBSPs. The simulated EBSP is used as reference pattern, with the parameters calibrated by IDIC3 and IDIC-D3 EBSD.

To single out the optical distortion effect in EBSD cameras from the above mentioned factors, chessboard-style standard samples could be applied on every camera to be tested, as done by Mingard *et al.* [32]. The method IDIC-D EBSD proposed here has the advantage of not requiring a calibration sample, and being fast and flexible.

5 Test on EBSPs taken by Bruker e$^-$Flash^{HD} camera 1

An EBSD dataset of a 70°-tilted unstrained polycrystal AlMg sample, captured by Bruker e$^-$Flash^{HD} detector with acceleration voltage 20kV and current 10nA, is analysed here. This dataset was first reported in Ref. [22]. The inverse pole figure of 10a shows that 5 grains are encompassed in the EBSD scan.

The IDIC-D method is applied on 30×40 EBSPs of definition 1200×1600. The radial distortion parameter for the sample calibrated by IDIC-D7 is shown in Figure 10b, and the map calibrated by IDIC-D4 in Figure 10d. The pattern center coordinates calibrated by IDIC-D7 are linearly fitted and fixed in the computation of IDIC-D4. Reducing the degrees of freedom from 7 to 4 results in a less noisy α map, but does not change the average values. The histograms of α for each grain are plotted in Figure 10c. The distribution of α is not identical for all 5 grains. Though the global α values are centered at 0, α are consistently positive or negative for some grains. For example, the EBSPs of grain 4 are calibrated with an average barrel distortion with $\alpha = 0.08 \times 10^{-8}$ pix^{-2}. The presence of more or less pronounced Kikuchi bands close the edge slightly varies from grain to grain and it is believed that this may be the origin of such a systematic effect. Note that this grain-wise α deviation is less than 3% of the common radial distortion values. This result demonstrates that the IDIC distortion correction method is generally

not significantly sensitive to the crystal orientations. This is a satisfactory feature, as the optical distortion behavior is an innate character for optical systems, and it should not vary with the samples being characterized.

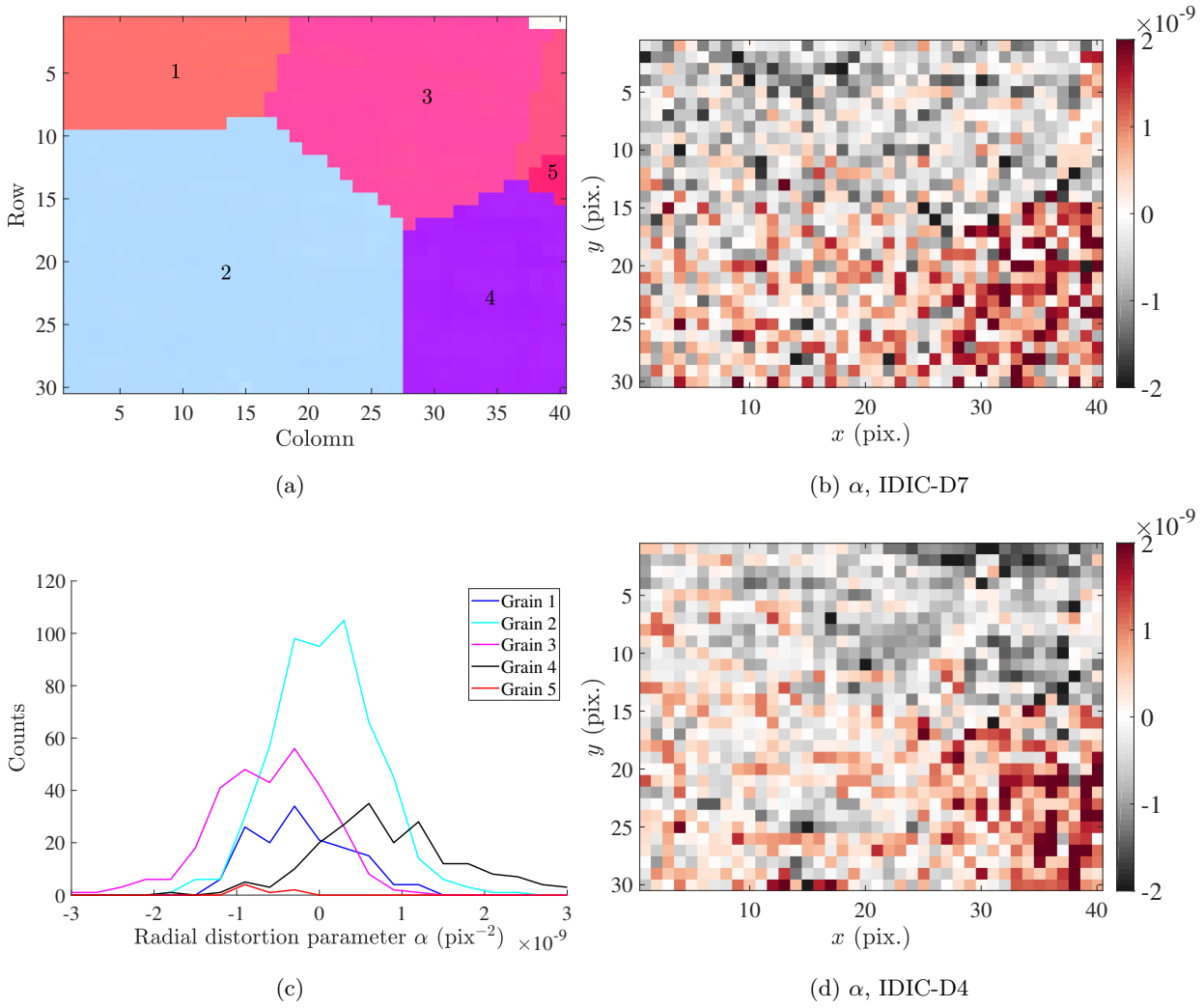

Figure 10: (a) The inverse pole figure of a polycrystal Al-Mg alloy. (b) The corresponding barrel distortion parameter α map by IDIC-D7. (c) The distribution of α values for each grain identified by IDIC-D4. (d) The α map by IDIC-D4.

Note that the estimated α in Figure 10b fluctuates in the range of 10^{-9}, roughly the noise level shown in Figure 7a. This result shows that the Bruker e^{-}Flash^{HD} camera used at our laboratory at Shanghai Jiao Tong University is free of radial distortions (up to our uncertainty).

6 Test on a TKD pattern taken by Bruker e^{-}Flash^{HD} camera 2

TKD has been increasingly used in materials characterization thanks to its better spatial resolution. The high resolution version of TKD provides strain and orientation maps of both high angular resolution and high spatial resolution [45]. The correction of optical distortion is also a necessary step for advanced analyses of TKD patterns.

A TKD pattern example for a cold-rolled Alloy600 (nickel matrix) is shown in Figure 11a. The pattern was acquired in a Zeiss Merlin SEM with Bruker's e$^-$Flash^{HD} detector installed at University of Oxford, with an accelerating voltage of 30kV and a probe current of 2nA.

The diffracting plane traces without radial distortion are shown in dashed lines, and the traces calculated by IDIC-D7 are plotted in solid lines. By scrutinizing the Kikuchi bands and the two diffracting line systems, one may find that the solid lines by IDIC-D7 lie more closely to the band central axes, especially for band 24 (whose location is highlighted in Figure 11b). Figure 11b shows the simulated TKD pattern by IDIC-D7 EBSD. Figure 11c shows the residual between the experimental pattern and the simulated one by IDIC-D7 EBSD. The numerous bright dots near the pattern center are the diffraction spots of the coherent incident electron beam. The weight of these bright dots is set to 0 in the ω field. Without any specific modification, IDIC(-D) EBSD can be applied on TKD dataset. The barrel parameter α is 2.78×10^{-8} pix^{-2} for the TKD, of the same magnitude as the reported values [32] and previously discussed values in Section 4. This result demonstrates that the IDIC-D is capable to correct the barrel distortion of transmission Kikuchi diffraction patterns.

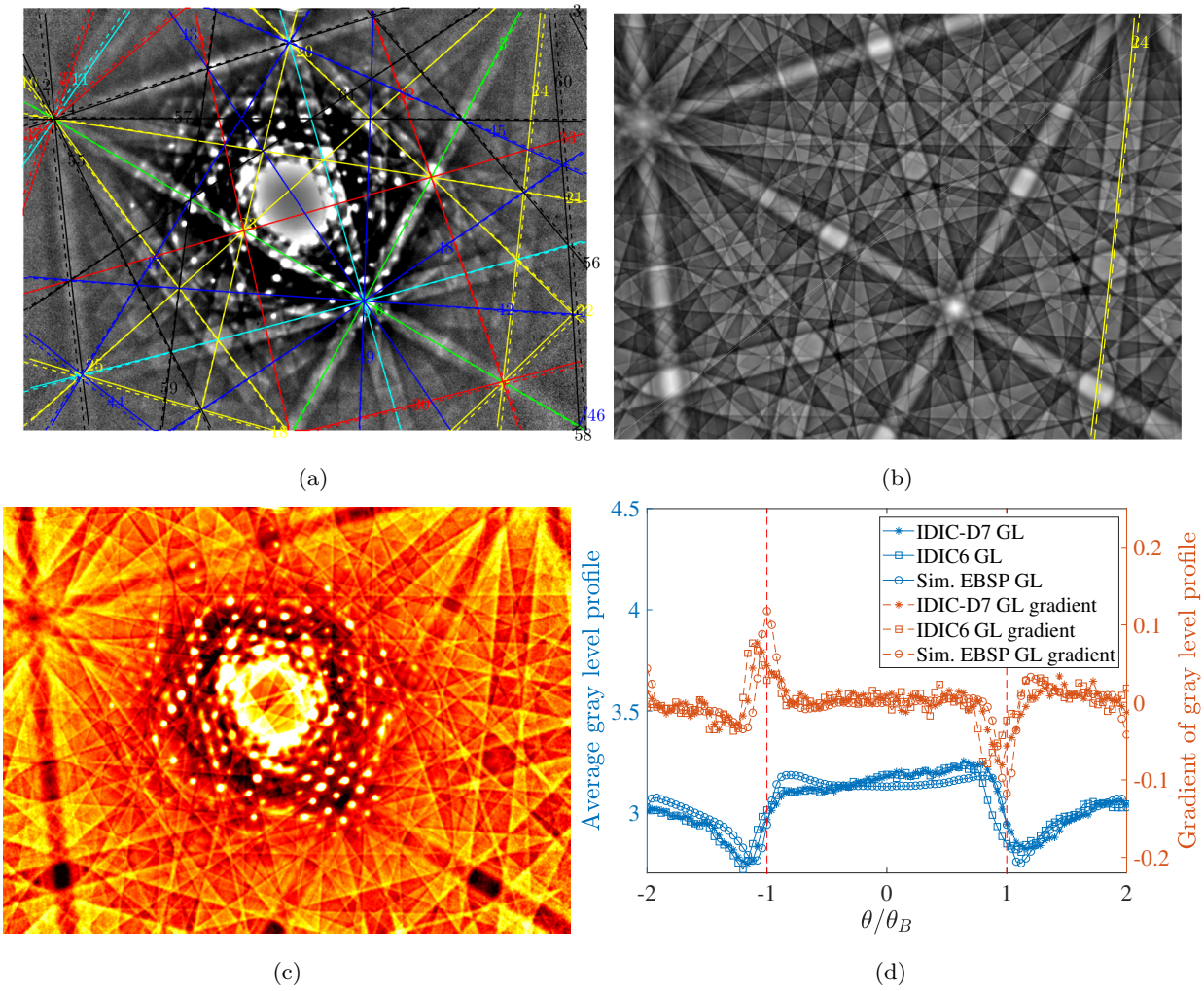

Figure 11: Barrel distortion correction for a TKD pattern. (a) The TKD pattern with the indexed Kikuchi band marked. (b) The simulated TKD pattern by IDIC-D EBSD. (c) The residual map between the TKD pattern and the projected master pattern. (d) shows the gray level profile of band 24 with the calibration results of IDIC EBSD and IDIC-D EBSD. The red dashed lines show the theoretical positions of the band edge.

The improvement of TKD indexation by IDIC-D over IDIC EBSD is visualized by the analysis of indexed band positions. The gray level (GL) profiles of K-band 24, for the experimental and simulated patterns, are plotted in Figure 11d. The calibration parameters of IDIC6 and IDIC-D7 are used to calculate the average GL profile of the experimental pattern separately. As stated before, the barrel distortion tends to shrink the peripheral part of the pattern. The profile of IDIC-calibrated parameters, shown in blue squares in Figure 11d, confirms this phenomenon as its width is smaller than the theoretical width. By correcting the barrel distortion, the pattern spreads in peripheral regions, as shown by the blue asterisks, and the width approaches the theoretical one for band 24.

The theoretical positions of the band edge given by Bragg's equation are plotted as dashed lines. As previous studies showed [46, 47], the location of highest gray level gradient coincides quite accurately with the true band edge. Correcting the optical distortion helps to move the experimental band to the expected position (*i.e.,* the position of the simulated pattern), as the peaks of brown asterisks are much closer to the theoretical position than

the brown squares in Figure 11d. IDIC-D has once more shown its ability to correct radial distortions.

Table 2 lists the radial distortion parameter α for the four cameras assessed by IDIC-D method. The uncertainty level indicated in the table corresponds to the standard deviation (std) of the measured data. Note that only 1 pattern is available from the camera Bruker e$^-$Flash^{HD}2, thus the uncertainty of α cannot be assessed. Besides, the uncertainty of the 3 former cameras should not be compared directly, as the radial distortion parameter of the Oxford Nordlys II camera is estimated from EBSPs of a single crystal, which probably underestimates the true uncertainty level.

Table 2: Summary of radial distortion assessed for the 4 cameras.

EBSP camera	Radial distortion parameter (10^{-8} pix^{-2})	Dataset nature
Nordif HR4M	0.728±0.042	20000 EBSPs from 3 grains
Oxford Nordlys II	3.08±0.05	5000 EBSPs from a single crystal
Bruker e$^-$Flash^{HD}1	0.00±0.08	1200 EBSPs from 5 grains
Bruker e$^-$Flash^{HD}2	2.78	A single TKD pattern

7 Conclusion

Full pattern match with simulated diffraction pattern has drawn increasing attention in advanced EBSD and TKD analyses, mainly thanks to its high precision. Accounting for numerous imperfect features of experimental electron diffraction patterns is vital to improve the accuracy, such as optical distortion, excess-deficiency effect of Kikuchi bands and inhomogeneous electron energy levels. This paper proposes to simultaneously estimate and correct the common radial distortion for electron diffraction patterns. By incorporating the radial distortion parameter into an integrated digital image correlation (IDIC) framework between experimental pattern and simulated master pattern, a variant algorithm IDIC-D manages to estimate the radial distortion and calibrate projection center (PC) without the need of specific standard hardware (i.e. chessboard sample).

Through 1 virtual test and 4 tests on high-resolution experimental EBSPs and transmission Kikuchi patterns, IDIC-D proves its ability to assess stably the radial distortion parameter. The correction of radial distortion on electron diffraction patterns has improved the EBSD indexation accuracy and the similitude between experimental and simulated patterns. The phantom strain values have reduced by 20-30% when using IDIC-D. The positioning of K-bands are more accurate, especially at the periphery of diffraction patterns. The adoption of radial distortion correction leads to more continuous projection center (PC) fields across grain boundaries, a strong evidence of the correctness of PC calibration. Failing to account for the radial distortion will deviate the PC from true value by 6-10 pixels (or 0.4-0.7% of the pattern width), especially for z^* as it is mainly affected by the zooming/de-zooming of radial distortion. IDIC-D algorithm solves the radial distortion problem at a negligible time cost, thus would bring beneficial effects on other advanced analyses of EBSD, such as the lattice constants estimation.

Appendix: Single crystal sample in 4-point flexural test

A 4-point flexural test has been performed by Emeric Plancher et. al. on a Zeiss Supra 55VP FEG-SEM operating at 20 kV with a probe current of 2.4 nA [6, 38]. A sample made of A316 stainless steel has been obtained by electric arc erosion from a single crystal ingot. The sample was orientated along the $\langle 100 \rangle$ axis with an uncertainty of 3°. Then the sample has been mechanically and electrochemically polished to minimize the surface residual stress. The final sample is of dimensions $30 \times 4.8 \times 0.5$ mm^3. It was tested by a 4-point flexural setup, which is illustrated in Figure 12. During the test the maximum force reached 5.4 N. A transverse profile has been studied to get its strain state, which is representative of the loading of the central part of the sample. Along this 500 µm long profile, HR-EBSD acquisitions have been performed over 5000 points, with a step size of 100 nm. The diffraction images have been recorded by a Nordlys II camera with a definition of 1344×1024 pixels.

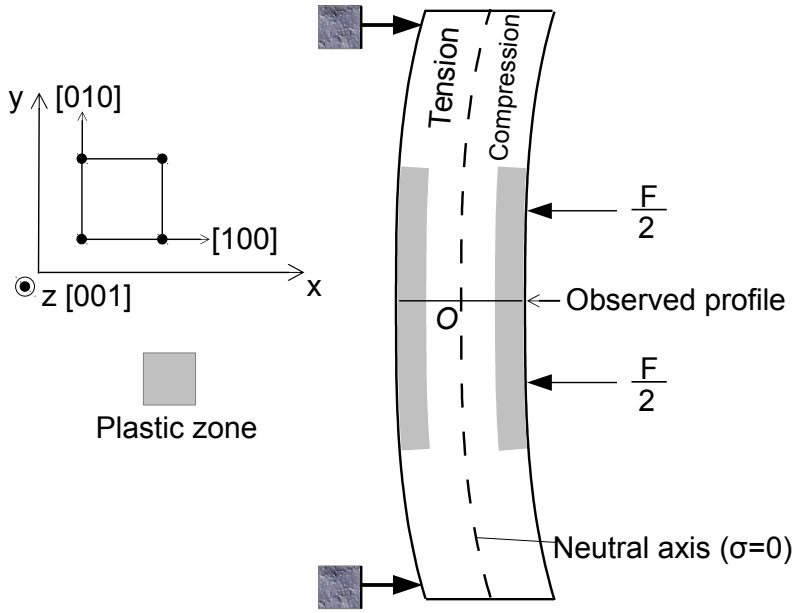

Figure 12: Sketch of 4-point flexural test [38].

Supplementary material: Slides of experimental and simulated diffraction patterns demonstrating the effect of radial distortion

Acknowledgements

This work is financially supported by the National Natural Science Foundation of China [No. 51901132, 52273229, 52101179]. We are also grateful to the financing from TESCAN CHINA, Ltd.

The hereby reported results correspond only to the 3 mentioned specific cameras. Due to the random variations of camera assembly, the results in this paper will not hold true even for the cameras of the same brands and series. This has been proven in the different radial distortion parameters for the two analysed Bruker e$^-$Flash^{HD} cameras. The authors do not have interest conflicts with the manufacturers of electron diffraction cameras reported in the

manuscript, and this paper should not be considered as a purchase guidance in camera selection.

Data Availability

The diffraction patterns of the unstrained polycrystal Al-Mg alloy are available at Zenodo (DOI: 10.5281/zenodo.6990325). The indexation results are also provided, including the crystal orientations, calibrated PC coordinates and the radial distortion parameter. The TKD pattern is shared by Phani Karamched at the website https://omg.web.ox.ac.uk/article/transmission-kikuchi-diffraction.

References

[1] S.I. Wright and B.L. Adams. Automatic analysis of electron backscatter diffraction patterns. *Metallurgical Transactions A*, 23(3):759–767, 1992.

[2] D. Jha, S. Singh, R. Al-Bahrani, W. Liao, A. Choudhary, M. De Graef, and A. Agrawal. Extracting grain orientations from EBSD patterns of polycrystalline materials using convolutional neural networks. *Microscopy and Microanalysis*, 24(5):497–502, 2018.

[3] Y.H. Chen, S.U. Park, D. Wei, G. Newstadt, M.A. Jackson, J.P. Simmons, M. De Graef, and A.O. Hero. A dictionary approach to electron backscatter diffraction indexing. *Microscopy and Microanalysis*, 21(3):739–752, 2015.

[4] A.J. Wilkinson, G. Meaden, and D.J. Dingley. High-resolution elastic strain measurement from electron backscatter diffraction patterns: New levels of sensitivity. *Ultramicroscopy*, 106(4-5):307 – 313, 2006.

[5] I. Brough, P. S. Bate, and F. J. Humphreys. Optimising the angular resolution of EBSD. 22(11):1279–1286, 2006.

[6] E. Plancher. *Full-field measurements of elastic and total strains for the determination of the local behaviour in polycrystals*. PhD thesis, Ecole nationale supérieure d'arts et métiers - ENSAM, December 2015.

[7] T. Vermeij and J.P.M. Hoefnagels. A consistent full-field integrated DIC framework for HR-EBSD. *Ultramicroscopy*, 191:44 – 50, 2018.

[8] T.J. Ruggles, G.F. Bomarito, R.L. Qiu, and J.D. Hochhalter. New levels of high angular resolution EBSD performance via inverse compositional Gauss-Newton based digital image correlation. *Ultramicroscopy*, 195:85 – 92, 2018.

[9] Q. Shi, S. Roux, F. Latourte, and F. Hild. Estimation of elastic strain by integrated image correlation on electron diffraction patterns. *Ultramicroscopy*, 199:16–33, 2019.

[10] C. Ernould, B. Beausir, J.-J. Fundenberger, V. Taupin, and E. Bouzy. Global DIC approach guided by a cross-correlation based initial guess for HR-EBSD and on-axis HR-TKD. *Acta Materialia*, 191:131 – 148, 2020.

[11] T. Vermeij, M. De Graef, and J. Hoefnagels. Demonstrating the potential of accurate absolute cross-grain stress and orientation correlation using electron backscatter diffraction. *Scripta Materialia*, 162:266 – 271, 2019.

[12] C. Maurice, R. Fortunier, J. Driver, A. Day, K. Mingard, and G. Meaden. Comments on the paper "Bragg's law diffraction simulations for electron backscatter diffraction analysis" by Josh Kacher, Colin Landon, Brent L. Adams and David Fullwood. 110(7):758 – 759.

[13] T.B. Britton, C. Maurice, R. Fortunier, J.H. Driver, A.P. Day, G. Meaden, D.J. Dingley, K. Mingard, and A.J. Wilkinson. Factors affecting the accuracy of high resolution electron backscatter diffraction when using simulated patterns. *Ultramicroscopy*, 110(12):1443 – 1453, 2010.

[14] D.A. Carpenter, J.L. Pugh, G.D. Richardson, and L.R. Mooney. Determination of pattern centre in EBSD using the moving-screen technique. *Journal of Microscopy*, 227(3):246–247, 2007.

[15] C. Maurice, K. Dzieciol, and R. Fortunier. A method for accurate localisation of EBSD pattern centres. *Ultramicroscopy*, 111(2):140 – 148, 2011.

[16] B.E. Jackson, J.J. Christensen, S. Singh, M. De Graef, D.T. Fullwood, E.R. Homer, and R.H. Wagoner. Performance of dynamically simulated reference patterns for cross-correlation electron backscatter diffraction. *Microscopy and Microanalysis*, 22(4):789–802, 2016.

[17] S. Vespucci, G. Naresh-Kumar, C. Trager-Cowan, K. P. Mingard, D. Maneuski, V. O'Shea, and A. Winkelmann. Diffractive triangulation of radiative point sources. *Applied Physics Letters*, 110(12):124103, 2017.

[18] G. Nolze, M. JÜrgens, J. Olbricht, and A. Winkelmann. Improving the precision of orientation measurements from technical materials via EBSD pattern matching. *Acta Materialia*, 159:408 – 415, 2018.

[19] E.L. Pang, P.M. Larsen, and C.A. Schuh. Global optimization for accurate determination of EBSD pattern centers. *Ultramicroscopy*, 209:112876, 2020.

[20] A. Foden, D.M. Collins, A.J. Wilkinson, and T.B. Britton. Indexing electron backscatter diffraction patterns with a refined template matching approach. *Ultramicroscopy*, 207:112845, 2019.

[21] T. Tanaka and A.J. Wilkinson. Pattern matching analysis of electron backscatter diffraction patterns for pattern centre, crystal orientation and absolute elastic strain determination - accuracy and precision assessment. *Ultramicroscopy*, 202:87–99, 2019.

[22] Q. Shi, D. Loisnard, C. Dan, F. Zhang, H. Zhong, H. Li, Y. Li, Z. Chen, H. Wang, and S. Roux. Calibration of crystal orientation and pattern center of EBSD using integrated digital image correlation. *Materials Characterization*, 178:111206, 2021.

[23] T. Friedrich, A. Bochmann, J. Dinger, and S. Teichert. Application of the pattern matching approach for EBSD calibration and orientation mapping, utilising dynamical EBSP simulations. *Ultramicroscopy*, 184:44 – 51, 2018.

[24] A. Winkelmann, B. Jablon, V. Tong, C. Trager-Cowan, and K. Mingard. Improving EBSD precision by orientation refinement with full pattern matching. *Journal of Microscopy*, 277(2):79–92, 2020.

[25] Q. Shi, Y. Zhou, H. Zhong, D. Loisnard, C. Dan, F. Zhang, Z. Chen, H. Wang, and S. Roux. Indexation of electron diffraction patterns at grain boundaries. *Materials Characterization*, 182:111553, 2021.

[26] A. Winkelmann and G. Nolze. Analysis of kikuchi band contrast reversal in electron backscatter diffraction patterns of silicon. *Ultramicroscopy*, 110:190–194, 2010.

[27] F. Ram and M. Graef. Energy dependence of the spatial distribution of inelastically scattered electrons in backscatter electron diffraction. *Physical review. B, Condensed matter*, 97:134104, 2018.

[28] Q. Shi, L. Jiao, D. Loisnard, C. Dan, Z. Chen, H. Wang, and S. Roux. Improved EBSD indexation accuracy by considering energy distribution of diffraction patterns. *Materials Characterization*, 188:111909, 2022.

[29] A. Winkelmann. Dynamical effects of anisotropic inelastic scattering in electron backscatter diffraction. *Ultramicroscopy*, 108(12):1546–1550, 2008.

[30] A. Winkelmann, G. Nolze, G. Cios, T. Tokarski, P. Bala, B. Hourahine, and C. Trager-Cowan. Kikuchi pattern simulations of backscattered and transmitted electrons. *Journal of Microscopy*, 284(2):157–184, 2021.

[31] J. Wang, F. Shi, J. Zhang, and Y. Liu. A new calibration model of camera lens distortion. 41(2):607–615, 2008.

[32] K. Mingard, A. Day, C. Maurice, and P. Quested. Towards high accuracy calibration of electron backscatter diffraction systems. *Ultramicroscopy*, 111(5):320 – 329, 2011.

[33] A.P. Day. Spherical EBSD. *Journal of Microscopy*, 230(3):472–486, 2008.

[34] C. Ernould, B. Beausir, J.-J. Fundenberger, V. Taupin, and E Bouzy. Integrated correction of optical distortions for global HR-EBSD techniques. *Ultramicroscopy*, page 113158, 2021.

[35] M. Islam, R. Lewis, K. Uesugi, and M. Kitchen. A high precision recipe for correcting images distorted by a tapered fiber optic. *Journal of Instrumentation*, 5:09008, 2010.

[36] W. Faig. Calibration of close-range photogrammetric systems: Mathematical formulation. *Photogrammetric Engineering and Remote Sensing*, 41, 1975.

[37] F. Hild and S. Roux. Digital image correlation. In P. Rastogi and E. Hack, editors, *Optical Methods for Solid Mechanics. A Full-Field Approach*, pages 183–228. Wiley-VCH, Weinheim (Germany), 2012.

[38] E. Plancher, J. Petit, C. Maurice, V. Favier, L. Saintoyant, D. Loisnard, N. Rupin, J.-B. Marijon, O. Ulrich, M. Bornert, J.-S. Micha, O. Robach, and O. Castelnau. On the accuracy of elastic strain field measurements by Laue microdiffraction and high-resolution EBSD: a cross-validation experiment. *Experimental Mechanics*, 56(3):483–492, 2016.

[39] E. Plancher, V. Favier, C. Maurice, E. Bosso, N. Rupin, J. Stodolna, D. Loisnard, J.-B. Marijon, J. Petit, J.-S. Micha, O. Robach, and O. Castelnau. Direct measurement of local constitutive relations, at the micrometre scale, in bulk metallic alloys. *Journal of Applied Crystallography*, 50(3):940–948, 2017.

[40] S. Singh, F. Ram, and M. De Graef. Emsoft: Open source software for electron diffraction/image simulations. *Microscopy and MicroAnalysis*, 23:S1:212–213, 2017.

[41] J. Alkorta. Limits of simulation based high resolution EBSD. *Ultramicroscopy*, 131:33 – 38, 2013.

[42] A. Koko, A. Wilkinson, and T. Marrow. An iterative method for reference pattern selection in high resolution electron backscatter diffraction (HR-EBSD), 2022. arXiv.2206.10242.

[43] D. Fullwood, M. Vaudin, C. Daniels, T. Ruggles, and S.I. Wright. Validation of kinematically simulated pattern HR-EBSD for measuring absolute strains and lattice tetragonality. *Materials Characterization*, 107(Supplement C):270 – 277, 2015.

[44] J. Alkorta, M. Marteleur, and P.J. Jacques. Improved simulation based HR-EBSD procedure using image gradient based DIC techniques. *Ultramicroscopy*, 182:17 – 27, 2017.

[45] C. Ernould, B. Beausir, J.-J. Fundenberger, V. Taupin, and E. Bouzy. Characterization at high spatial and angular resolutions of deformed nanostructures by on-axis HR-TKD. *Scripta Materialia*, 185:30 – 35, 2020.

[46] N. Saowadee, K. Agersted, and J. Bowen. Lattice constant measurement from electron backscatter diffraction patterns. *Journal of Microscopy*, 266(2):200–210, 2017.

[47] G. Nolze, T. Tokarski, Ł. Rychłowski, G. Cios, and A. Winkelmann. Crystallographic analysis of the lattice metric (CALM) from single electron backscatter diffraction or transmission Kikuchi diffraction patterns. *Journal of Applied Crystallography*, 54(3):1012–1022, 2021.

Experimental EBSP of 4-point bend stainless steel

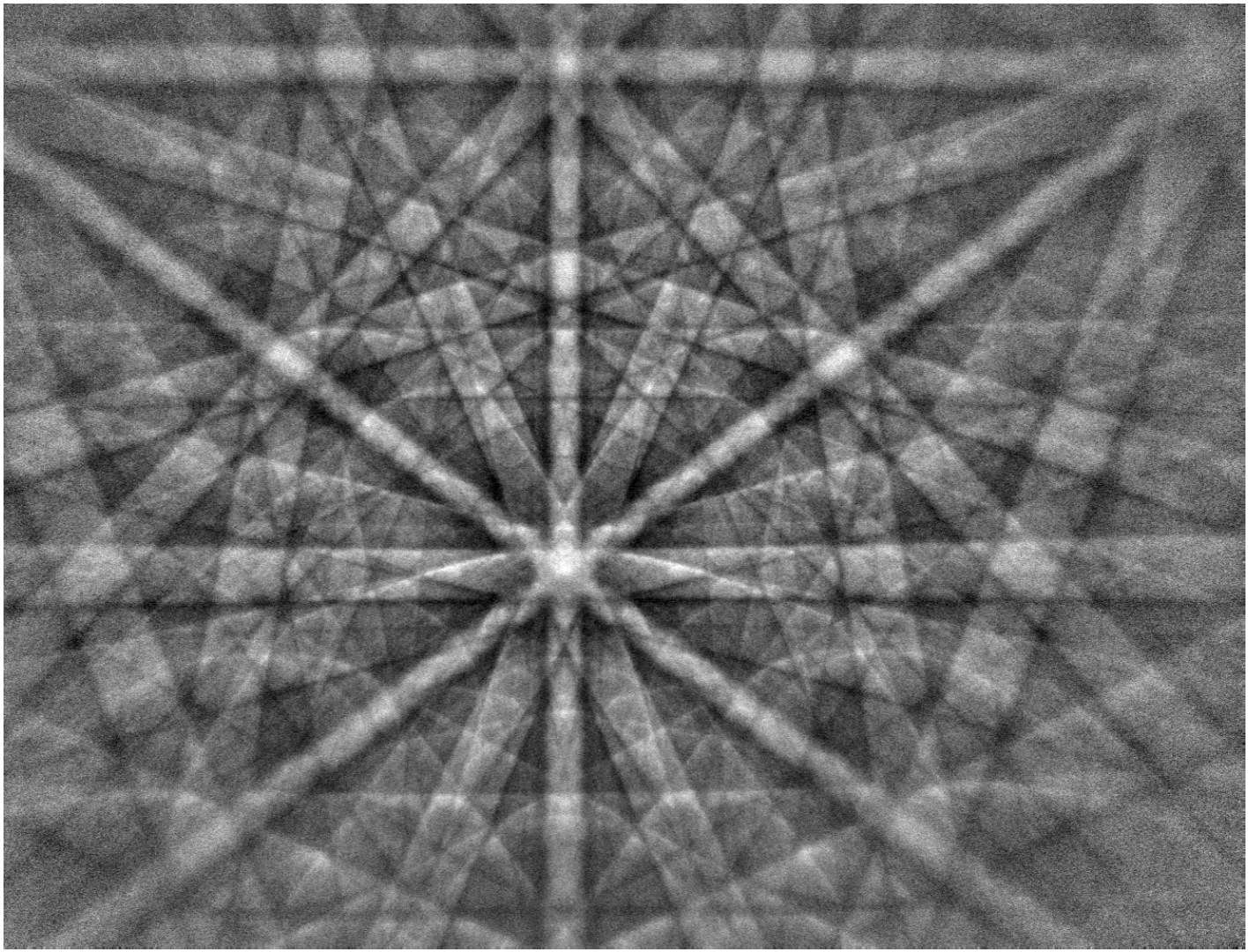

Simulated EBSP with barrel distortion: $\alpha = 3.08 \times 10^{-8}$

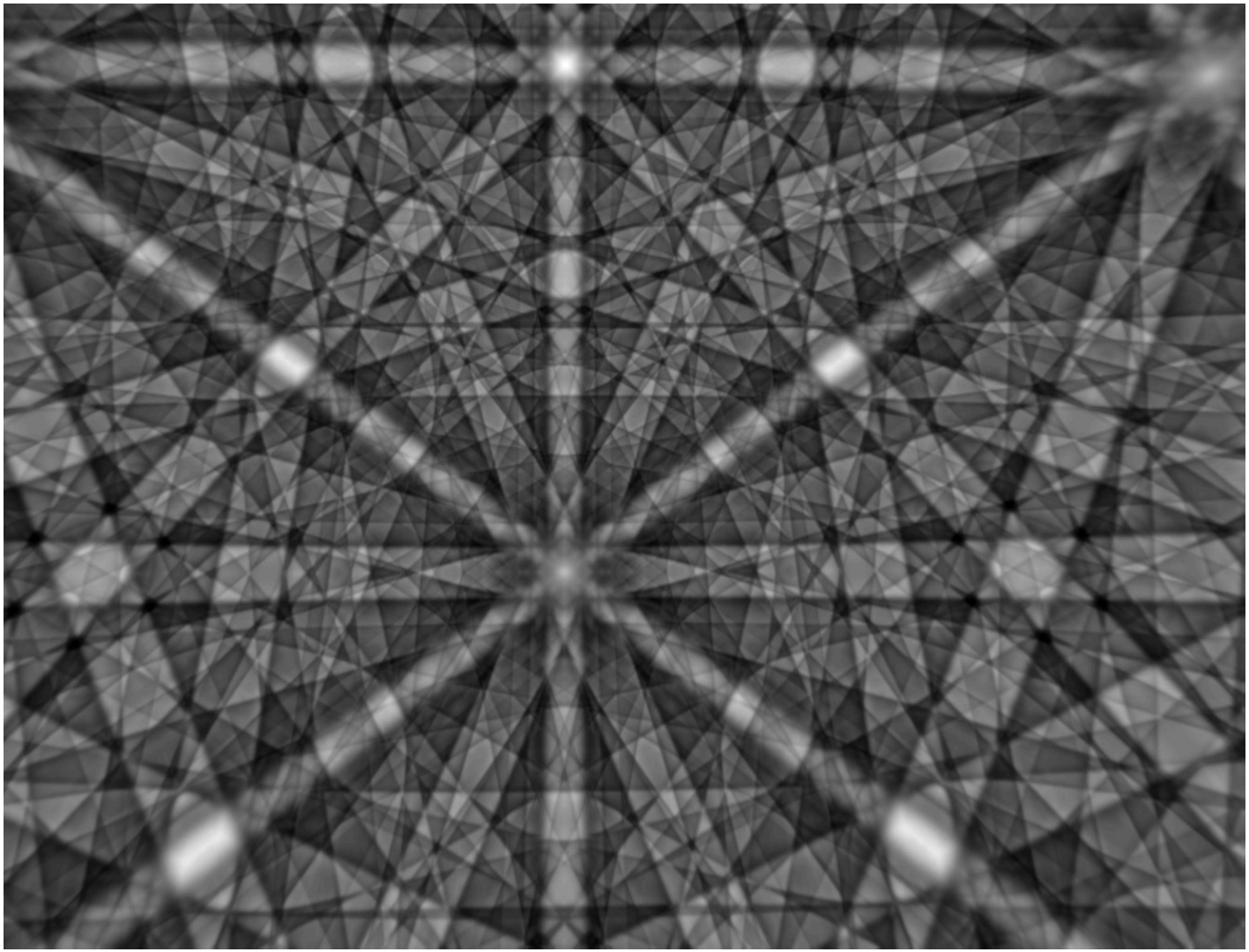

Simulated EBSP without distortion

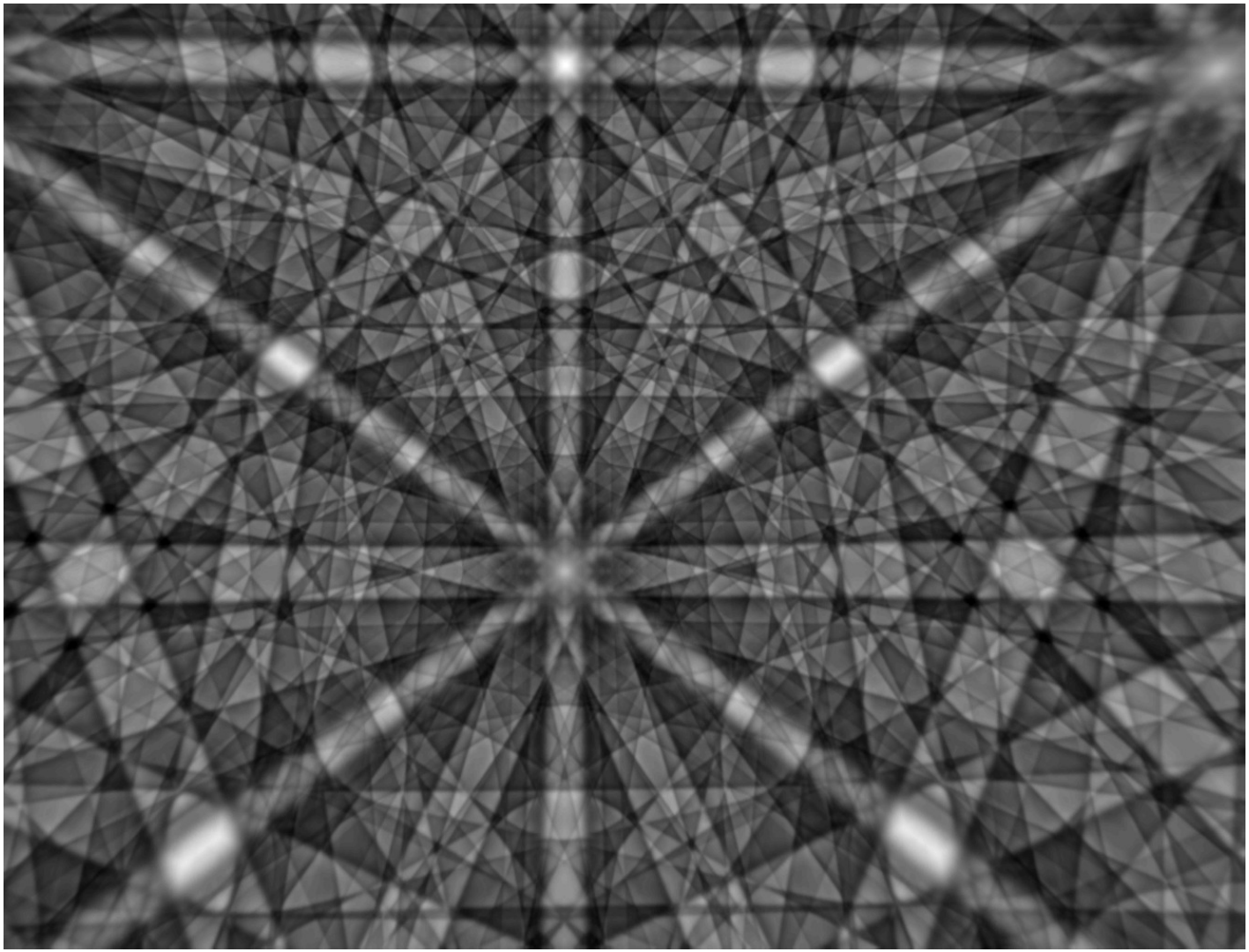

Dots + bands: TKD pattern of cold-rolled Alloy600

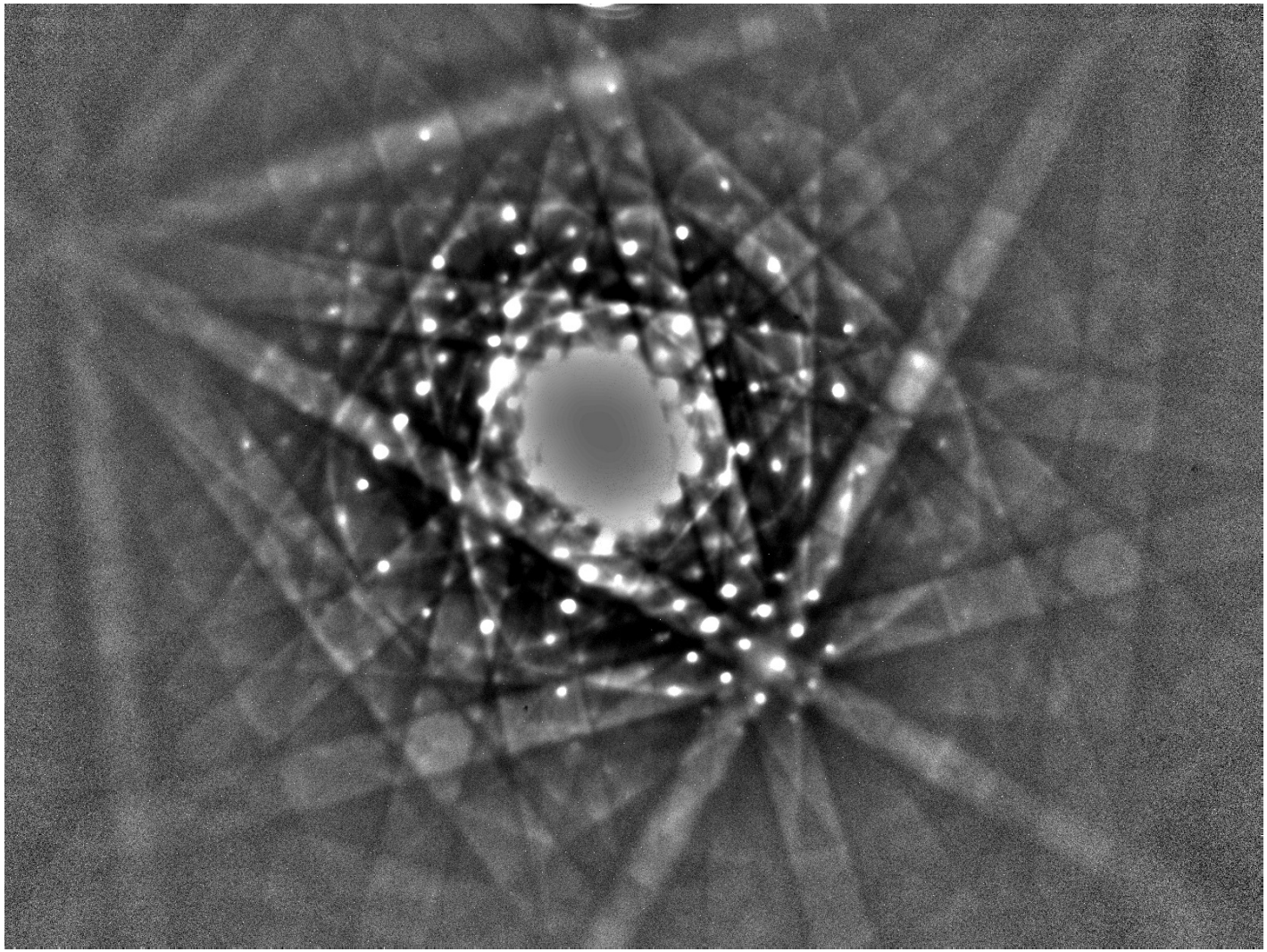

Simulated pattern with barrel distortion ($\alpha = 2.78 \times 10^{-8}$)

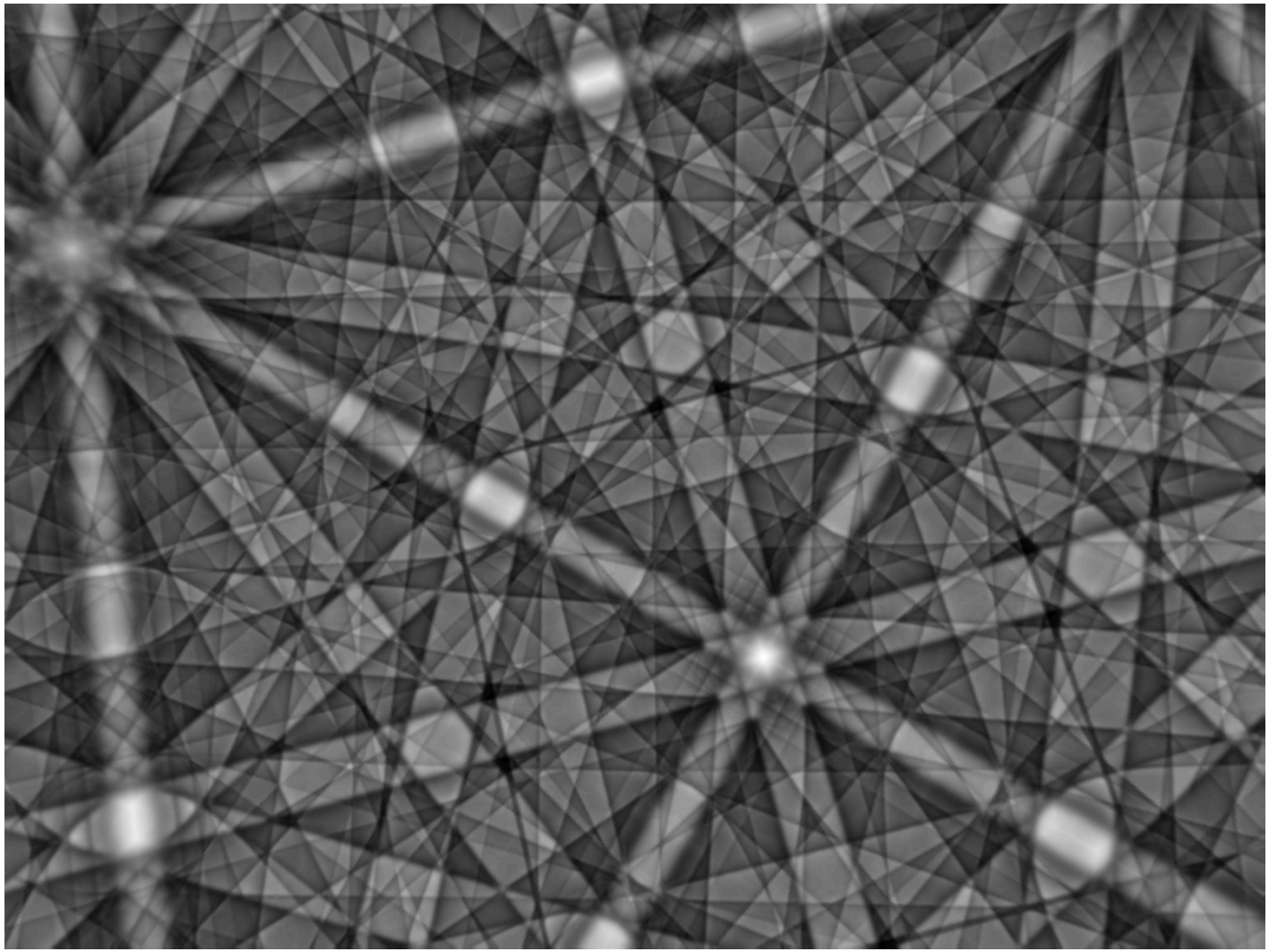

Simulated pattern assuming no radial distortion